Cellular Automata and Anisotropic Diffusion Filter based Interactive Tumor Segmentation for Positron Emission Tomography

Lei Bi, Jinman Kim, *Member, IEEE*, Lingfeng Wen, *Member, IEEE,* Ashnil Kumar*, Student Member, IEEE,* Michael Fulham and David Dagan Feng, *Fellow, IEEE*

Abstract— **Tumor segmentation in positron emission tomography (PET) aids clinical diagnosis and in assessing treatment response. However, the low resolution and signal-to-noise inherent in PET images, makes accurate tumor segmentation challenging. Manual delineation is time-consuming and subjective, whereas fully automated algorithms are often limited to particular tumor types, and have difficulties in segmenting small and low-contrast tumors. Interactive segmentation may reduce the inter-observer variability and minimize the user input. In this study, we present a new interactive PET tumor segmentation method based on cellular automata (CA) and a nonlinear anisotropic diffusion filter (ADF). CA is tolerant of noise and image pattern complexity while ADF reduces noise while preserving edges. By coupling CA with ADF, our proposed approach was robust and accurate in detecting and segmenting noisy tumors. We evaluated our method with computer simulation and clinical data and it outperformed other common interactive PET segmentation algorithms.**

I. Introduction

Accurate tumor segmentation from positron emission tomography (PET) images plays a pivotal role in clinical diagnosis and in assessing therapy response [1]. However, tumor segmentation for PET images is challenging due to poor resolution and low signal-to-noise ratio (SNR) inherent in PET [2, 3]. Efforts have been made for developing new segmentation algorithms to address the issues in manual delineation, which is time consuming and operator dependent with high inter- and intra-observer variability [4]. Automated approaches [4-6], such as fuzzy C-means [4], adaptive region growing and dual-front active contour [5], have demonstrated their performances in segmenting tumors. However, these approaches are often limited to simulations [6] and to particular types of tumors, e.g., non-small cell lung cancer (NSCLC) [4] and head-and-neck tumor [5]. These fully automated approaches also may not be able to provide sufficiently accurate and robust PET tumor segmentation for small (e.g., 15 pixel volume) and/or low-contrast (e.g., 2:1 tumor to background) tumors [4].

L. Bi, J. Kim, L. Wen, A. Kumar, and D. Feng are with the School of Information Technologies, University of Sydney, NSW, Australia. L. Bi (e-mail: lei@it.usyd.edu.au); J. Kim (e-mail: jinman.kim@sydney.edu.au); A. Kumar (e-mail: ashnil@it.usyd.edu.au).

L. Wen and M. Fulham are with Department of Molecular Imaging, Royal Prince Alfred Hospital, NSW, Australia. L. Wen (e-mail: wenlf@ieee.org).

M. Fulham is also with the Sydney Medical School, University of Sydney, NSW, Australia (e-mail: michael.fulham@sydney.edu.au).

D. Feng is also with CMSP, Department of EIE, Hong Kong Polytechnic University, Hong Kong, and Med-X Research Institute, Shanghai Jiao Tong University, China (e-mail: dagan.feng@sydney.edu.au).

Interactive segmentation algorithms that combine prior knowledge of operators with pattern recognition techniques offer an ideal alternative to overcome the limitations of manual or fully automated algorithms [7]. Region-based algorithms have been widely used [5, 8, 9] for interactive PET tumor segmentation due to their simplicity and performance. In the conventional seeded region growing (SRG) algorithm [10], users are only required to select a set of seeds (fore- and background); unallocated neighboring pixels are iteratively merged to the region grown from the seeds according to the similarity of pixel intensities. In the work of Day et al [8], the application of confidence connected region growing (CCRG) algorithm was presented for PET; the pixel merging criteria is based on the mean and the standard deviation of pixel intensities. The CCRG was also used on temporal PET segmentation in [11].

In this study, we propose a new PET tumor segmentation method by combining cellular automata (CA) and a nonlinear anisotropic diffusion filter (ADF). Our method is designed to counter the noise and low SNR in PET and enable segmentation of small and low-contrast tumors in a simple and interactive manner. The CA model has been proposed for interactive region-based segmentation in medical imaging [12-14]. It is based on a lattice of 'cells' (pixels), which are assigned to the fore- and back-ground (user selected) or undefined. Each iteration of the algorithm, the cells propagate across the whole lattice according to the cell's features. CA has been shown to be tolerable to noise and image pattern complexity with minimum user interactions in medical images. We couple CA with ADF to reduce noise while preserving edges [15]. The ADF is based on a non-linear diffusion equation to estimate a piecewise constant image from a noisy input image, which avoids blurring edges and other localization problem [4].

The performance of our proposed CA-ADF method was evaluated using simulation and clinical data by comparing results of other region-based PET segmentation of CCRG [8, 11] , SRG [10] and the Otsu thresholding algorithm [16].

II. Methods and Materials

A. Proposed CA-ADF Segmentation

1) Cellular Automata

A cellular automata model can be defined as a triplet $A = (S, N, \delta)$ where S is a non-empty state set, N is the neighborhood system, and $\delta: S^N \to S$ is the transition function. The function defines the rule of calculating the cell's state at time $t + 1$ based on the states of its neighborhood cells at time t. In our study, pixels from PET

images are considered as cells and we used Moore's neighborhoods, n, set to 26 pixels [12]:

$$N(p) = \{q \in Z^n : \|p - q\|_\infty := \max_{i=1,n} |p_i - q_i| = 1\} \quad (1)$$

where pixel q is a neighbor of pixel, p, where $p \in P$. The cell state S_p is a triplet (l_p, θ_p, I_p), where the state of the p is defined as the label, l_p, which is set to 1 for the foreground and 2 for the background; θ_p is the strength, where $0 \le \theta_p \le 1$, and I_p is the feature vector, used it to represent the intensity value of p. Initially for each seed, p_{seed}, the state is set as:

$$l_{p_{seed}} = \begin{cases} 1 \ if \ p_{seed} \in foreground \\ 2 \ if \ p_{seed} \in background \end{cases}, \theta_{p_{seed}} = 1. \quad (2)$$

The segmentation assigns unlabeled pixels based on the transition function following the pseudo code below [14]:

```
//For each cell …
for ∀p∈ P
    //copy previous state
    l_p^{t+1} = l_p^t
    θ_p^{t+1} = θ_p^t
    //Neighbors try to attack current cell
    for ∀q∈ N(p)
        if g(|I_p − I_q|) · θ_q^t > θ_p^t
            l_p^{t+1} = l_q^t
            θ_p^{t+1} = g(|I_p − I_q|) · θ_q^t
        end if
    end for
end for
```

where g is a monotonically decreasing function bounded by [0, 1] and defined as:

$$g(x) = 1 - \frac{w_p \cdot x}{max|I|} \quad (3)$$

and w_p is a weight function applied to smooth the pixels in the neighborhood according to:

$$w_p = \frac{1}{1 + \sqrt{\frac{1}{n}\sum_{q=1}^{n}(I_p - I_q)^2}} \quad (4)$$

The process continues until there are no further changes in all the pixel states.

2) Anisotropic diffusion filter

A nonlinear anisotropic diffusion filter (ADF) was applied prior to the CA. An ADF filter can be defined as [4]:

$$\partial P_\tau = div(g(\|\nabla P\|)\nabla P), \qquad P(0) = P_0 \quad (5)$$

where P_0 is the original image, P is the denoised image, ∂P_τ is the partial derivative of P with respect to diffusion time τ, div denotes the divergence operator and $\|\nabla P\|$ is the gradient magnitude of P. We adopted the diffusivity function $g(\|\nabla P\|)$ as in Tschumperle's work [15], where homogenous regions are smoothed isotropically and edges regions are smoothed anisotropically. The resulting image provides stable edges even after a large number of iterations.

3) Interactive Bounding Box

The only user interaction required was for initializing the segmentation process. A user defined a bounding box (x- and y-axis) that completely encapsulated the tumor on a single slice. Using this box, the z-axis (depth) was calculated to be the average of its width and height. All sides were then expanded by a buffer (2 to 4 pixels). Peak intensity was then derived from the given bounding box and pixels were assigned as the foreground seeds set if their intensity were ≥

50% of the peak. The 26 pixels belonging to the corners and middle of edges of the box, if not already classified as the foreground, were then added to the background seeds set.

B. Other PET Segmentation Algorithms

Common interactive region-based PET segmentation algorithms of CCRG [8, 11] and SRG [10] were used for the comparative evaluation. The same bounding box and the seeds sets from Section 2.1.3 were used. As a reference to the most popular type of PET segmentation algorithm, we further compared to thresholding algorithm of Otsu [16] .

C. Materials
1) Simulation Dataset

The OncoPET database [17] of simulated PET studies of lymphoma was used. Each study consisted of 375 slices at a thickness of 2.4mm with 128×128 matrix at the pixel resolution of 5.06×5.06mm^2. In total, 25 studies were used with 54 spherical tumors in total, resided either in blood pool, lungs, liver or spleen. Prior to reconstruction, the diameters of the tumors were predefined to be 3 or 4 pixels with contrast ratios of 2:1 to 10:1 (tumor: background).

2) Clinical Dataset

For our evaluation, we randomly selected thirteen clinical whole-body FDG-PET studies, all diagnosed with non-small-cell lung cancer (NSCLC). They were acquired at the Department of PET and Nuclear Medicine, Royal Prince Alfred (RPA) hospital with a Siemens Biograph TruePoint PET-CT scanner were used for evaluation. All PET studies had 326 slices at a thickness of 3mm to cover the body from the top of the head to the upper thigh. Each slice had a 200×200 matrix at a pixel resolution of 4.07×4.07mm^2. 6 studies had two or more separable lung tumors, while others had a single lung tumor. In total, there were 29 tumors with volumes ranging from 12 to 1200 pixels.

D. Evaluation

The results were evaluated by comparing the generated segmentation labels with the available ground truth. Dice similarity coefficient (DSC) was used to measure the overlap between the two volumes [18] according to:

$$DSC = \frac{2N(A\cap B)}{N(A)+N(B)} \quad (6)$$

where A and B represent binary labels of the segment label and the ground truth, respectively, and N indicates the number of pixels in the corresponding set. For the CA-ADF, SRG and Otsu algorithms, apart from the user-defined bounding box (Section 2.1.3), no other parameters were set. For the CCRG, standard deviation was needed to be defined as convergence criteria which we empirically derived to be 0.8 (varied from 0.6 to 1.2 with the increment of 0.2) for both the clinical and simulation studies.

1) Simulation data

The OncoPET simulation dataset was used to evaluate the segmentation algorithms in detecting small and low-contrast tumors. Tumors were spread across different structures, often in close proximity to other high uptake structures, e.g., heart and blood pool. The simulation has absolute location and the diameter of the tumors as the ground truth, prior to reconstruction, thus providing an estimate that can be used to

measure tumor detectability. In our evaluation, we counted the number of occurrences when the DSC result was above certain accuracy, measured from $\geq 40\%$ (in increments of 5%). In our results, $DSC \leq 40\%$ was considered to be unsuccessful detection of tumors. The initial bounding box was constructed based on the size of the truth with +2 pixel buffer in all directions to ensure that the tumors were completely encapsulated while separated to the background.

2) Clinical PET Data

For clinical studies, we followed the suggestion of defining the tumor regions using a threshold-based algorithm [19]. Manual tumor delineation by experts, which has high inter- and intra-observer variability, was not used in this study. Instead, we used PET response criterion (PERCIST) [20] thresholding algorithm, supplemented with clinical reports of tumor findings, to derive the tumors as the ground truth. PERCIST is well accepted in its use to derive metabolic changes of malignant lesions in assessing treatment response. For our experiments, the bounding box for each of the tumors was set to the size of the tumors from the ground truth with the addition of +4 pixels in all directions.

III. RESULTS AND DISCUSSION

A. Simulation Results

Figure 1 plots the accumulation of successfully detected tumors when the accuracy was varied from $\geq 40\%$ to $\geq 85\%$ (the highest accuracy was < 85%), e.g., the CA-ADF had 10 tumors correctly detected when the segmentation results had $DSC \geq 60\%$. Among the four compared algorithms, CA-ADF was most robust on correctly detecting the tumors. Table I presents the segmentation results, where CA-ADF had the highest average of 0.41 and also the highest accuracy of 0.84. The low DSC accuracy for all four algorithms is expected since the reconstructed OncoPET images significantly enlarges the tumor size ($\sim 2\times$) from the original simulation due to partial volume effects and small tumor sizes. Nevertheless, it provides absolute ground truth reference to the tumor location which was used in this evaluation.
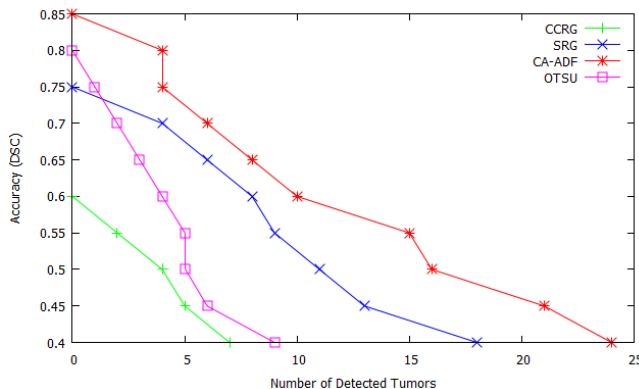

Figure 1. Accumulated detected tumor cases.

Table I. DSC results of simulation PET image segmentation.

	CCRG	SRG	CA-ADF	Otsu
Average	0.17	0.38	0.41	0.31
SD	0.18	0.16	0.20	0.16
Max	0.56	0.74	0.84	0.75
Min	0	0.17	0.15	0

To assess the influence of the contrast to the accuracy of the segmentation results, the failed cases (DSC < 40%) were separatelylisted in Table II based on their contrast ratios. The table shows that CA-ADF consistently performed better across all contrast ratios. CA-ADF clearly outperformed the other algorithms when the contrast ratio was 5:1, which corresponded to a tumor located within the blood pool. Figure 2 shows an example of segmentation results.

Table II. Count of failures among different contrast ratios

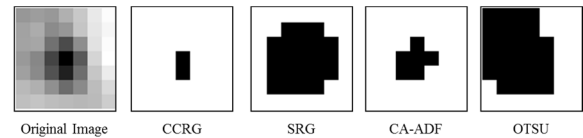| Contrast Ratios	CCRG	SRG	CA-ADF	Otsu
2:1	2	2	2	2
2.5:1	9	7	7	9
3:1	8	8	7	9
4:1	11	6	6	8
4.5:1	2	2	2	2
5:1	9	8	4	9
7.5:1	3	0	0	3
8:1	1	1	1	1
10:1	2	2	1	2

Figure 2. Segmentation of a simulated tumor (contrast ratio of 5:1) located within the blood pool consisting of inconsistent surrounding tissues as shown in the Original Image. Images are scaled at $\times 16$.

B. Clinical Results

Table III presents the segmentation results for the 13 clinical PET studies using DSC measures. CA-ADF had the highest average of 0.77, lowest standard deviation of 0.20 and best minimum accuracy of 0.22. Both CA-ADF and Otsu had the highest Max accuracy of 0.96.

Table III. DSC results of clinical PET image segmentation.

	CCRG	SRG	CA-ADF	Otsu
Average	0.53	0.55	0.77	0.73
SD	0.24	0.23	0.20	0.28
Max	0.91	0.91	0.96	0.96
Min	0.11	0.11	0.22	0.07

Generally, Otsu performed well with high-contrast tumors, but failed in tumors which had multiple peaks in their intensity distributions. Further, typical of a thresholding algorithm, Otsu was unable to separate the tumor from other high uptake regions, resulting in the lowest minimum accuracy, as in Figure 3a. Figure 3b shows that CA-ADF was capable of correct segmentation of the tumor while CCRG suffered from under-segmentation and SRG was over-segmented. Figure 4 further exemplifies the CA-ADF results on a patient with two tumors in the lungs. The CA-ADF was able to depict the small tumor (55 pixels; DSC of 0.96) and also a larger but irregularly shaped tumor (111 pixels; DSC of 0.75).
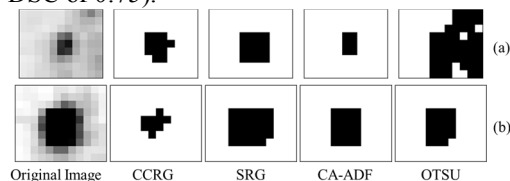

Figure 3. Clinical PET tumor segmentations. Images scaled at $\times 12$.

(a) PET Image   (b) Original Image   (c) CA-ADF   (d) Original Image   (e) CA-ADF
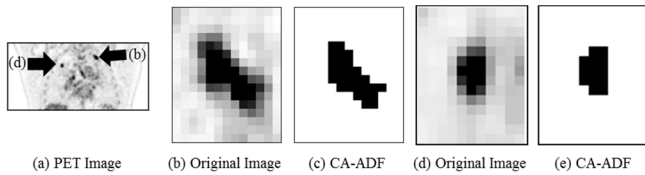
Figure 4. PET tumor segmentation from a non small-cell lung cancer (NSCLC) study with our CA-ADF algorithm. (a) shows two tumors of varying sizes and shape complexities. (b) depicts the larger tumor inside its bounding box (cropped) with the result in (c). (d) and (e) presents the other smaller tumor. Images are scaled ×8.

We evaluated the robustness of CA-ADF with two different bounding box sizes as shown in Figure 5. In this example, the larger box included parts of non-tumor structures that had high-uptake pixels (the myocardium) in Figure 5 (a) but still successfully segmented the tumor with consistent DSC results (< 0.1% difference) when compared to the smaller box result.
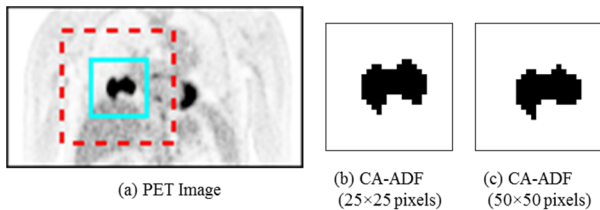

(a) PET Image   (b) CA-ADF (25×25 pixels)   (c) CA-ADF (50×50 pixels)

Figure 5. CA-ADF segmentation results for the smaller box (blue in (a)) are shown in (b) and a larger box (red dotted) in (c). Images are scaled ×6.

C. Computational Cost

All segmentations were done on a PC with Intel Core i7 3.4GHz CPU and 16GB RAM. Table IV lists the computational cost of the tumor segmentation on clinical studies with the CA-ADF having an average time of 0.60 seconds to segment a tumor, prior to code optimization. Comparatively, CCRG and SRG resulted in results of 0.50 and 0.45 seconds.

Table IV. Computational costs of CA-ADF segmentation

	Computation Time (Seconds)	Bounding Box Size (Pixels)
Average	0.60	2928
Min	0.35	660
Max	1.56	12121
SD	0.28	2717

IV. CONCLUSION AND FUTURE WORK

In this study, we presented a new interactive PET tumor segmentation algorithm based on cellular automata and an anisotropic diffusion filter that only required the manual selection of a bounding box. The simulation and clinical results show that our proposed CA-ADF had higher segmentation accuracy than other commonly used region-based interactive segmentation algorithms used in PET. As our future work, we will improve the interactivity in the seed selection and evaluate our segmentation on greater variety of tumor cases.

ACKNOWLEDGEMENT

REFERENCES

[1] Mathieu. Hatt, et al. "A fuzzy locally adaptive Bayesian segmentation approach for volume determination in PET." *IEEE T. Med. Imag.*, 28.6, 881-893, 2009..

[2] H. Zaidi, et al., "PET-guided delineation of radiation therapy treatment volumes: a survey of image segmentation techniques," *Eur. J. Nucl. Med. Mol.,* vol. 37, pp. 2165-87, 2010.

[3] J. Kim, et al., "Automatic 3D temporal kinetics segmentation of dynamic emission tomography image using adaptive region growing cluster analysis," *IEEE. Conf. Nucl. Sci.,* pp. 1580-3, 2002.

[4] S. Belhassen, et al., "A novel fuzzy C-means algorithm for unsupervised heterogeneous tumor quantification in PET," *Med. Phys.,* vol. 37, p. 1309, 2010.

[5] H. Li, et al., "A novel PET tumor delineation method based on adaptive region-growing and dual-front active contours," *Med. Phys.,* vol. 35, p. 3711, 2008.

[6] E. Prieto, et al., "Twelve automated thresholding methods for segmentation of PET images: a phantom study," *Phys. Med. Biol.,* vol. 57, p. 3963, 2012.

[7] P. A. Freeborough, et al., "Interactive algorithms for the segmentation and quantitation of 3-D MRI brain scans," *Comput. Meth. Prog. Bio.,* vol. 53, pp. 15-25, 1997.

[8] E. Day, et al, "A region growing method for tumor volume segmentation on PET images for rectal and anal cancer patients," *Med. Phys.,* vol. 36, p. 4349, 2009.

[9] J. Kim, et al., "Segmentation of VOI from multidimensional dynamic PET images by integrating spatial and temporal features," *IEEE Trans. Info. Tech. Biome.,* vol. 10, pp. 637-46, 2006.

[10] R. Adams, et al., "Seeded region growing," *IEEE T. Pattern. Anal.,* vol. 16, pp. 641-7, 1994.

[11] G. Nyirenda, et al., "Automated segmentation of tumour changes in temporal PET-CT data," *IEEE. I. S. Biomed. Imaging.,* pp. 1699-1702, 2012.

[12] V. Vezhnevets, et al., "GrowCut: Interactive multi-label ND image segmentation by cellular automata," *Proc. of Graphicon,* pp. 150-6, 2005.

[13] Y. Liu, et al., "An effective approach of lesion segmentation within the breast ultrasound image based on the cellular automata principle," *J. Digit. Imaging.,* pp. 1-11, 2012.

[14] A. Hamamci, et al., "Tumor-Cut: Segmentation of Brain Tumors on Contrast Enhanced MR Images for Radiosurgery Applications," *IEEE T. Med. Imag.,* vol. 31, pp. 790-804, 2012.

[15] D. Tschumperle, et al., "Vector-valued image regularization with PDEs: A common framework for different applications," *IEEE. T. Pattern. Anal.,* vol. 27, pp. 506-17, 2005.

[16] N. Otsu, "A threshold selection method from gray-level histograms," *Automatica,* vol. 11, pp. 23-7, 1975.

[17] S. Tomei, et al., "OncoPET_DB: a freely distributed database of realistic simulated whole body 18F-FDG PET images for oncology," *IEEE T. Nucl. Sci.,* vol. 57, pp. 246-55, 2010.

[18] W. R. Crum, et al., "Generalized overlap measures for evaluation and validation in medical image analysis," *IEEE T. Med. Imag.,* vol. 25, pp. 1451-61, 2006.

[19] S. David, et al., "Multi-observation PET image analysis for patient follow-up quantitation and therapy assessment," *Phys. Med. Biol.,* vol. 56, p. 5771, 2011.

[20] R. L. Wahl, et al., "From RECIST to PERCIST: evolving considerations for PET response criteria in solid tumors," *J. Nucl. Med.,* vol. 50, pp. 122S-50S, 2009.